AD-A149 336 SURFACE STRUCTURE ANALYSIS USING LOW ENERGY ION SCATTERING I CLEAN FE(001..(U) PENNSYLVANIA UNIV PHILADELPHIA DEPT OF MATERIALS SCIENCE AND E.. 1/1

UNCLASSIFIED L MARCHUT ET AL. 1984 TR-28 F/G 7/4 NL

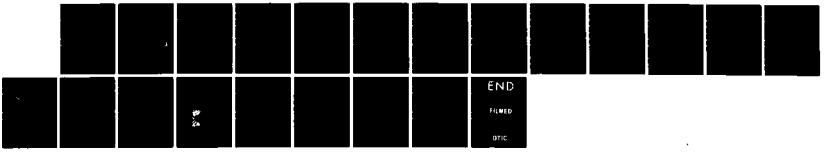

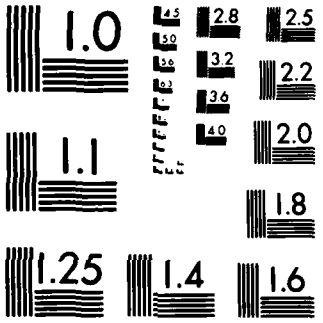

MICROCOPY RESOLUTION TEST CHART
NATIONAL BUREAU OF STANDARDS-1963-A

UNCLASSIFIED

SECURITY CLASSIFICATION OF THIS PAGE (When Data Entered)

REPORT DOCUMENTATION PAGE	READ INSTRUCTIONS BEFORE COMPLETING FORM
1. REPORT NUMBER: Technical Report No. 28 — 2. GOVT ACCESSION NO.	3. RECIPIENT'S CATALOG NUMBER
4. TITLE (and Subtitle): Surface Structure analysis using low energy ion scattering I. Clean Fe(001)	5. TYPE OF REPORT & PERIOD COVERED
	6. PERFORMING ORG. REPORT NUMBER
7. AUTHOR(s): L. Marchut, T.M. Buck, G.H. Wheatley and C.J. McMahon, Jr.	8. CONTRACT OR GRANT NUMBER(s): N00014-83-K-0565
9. PERFORMING ORGANIZATION NAME AND ADDRESS: Trustees of the Univ. of Pennsylvania, Office of Projects Research and Grants, 3451 Walnut St., Philadelphia, PA 19104	10. PROGRAM ELEMENT, PROJECT, TASK AREA & WORK UNIT NUMBERS: NR 629-844/6-08-84 (410)
11. CONTROLLING OFFICE NAME AND ADDRESS: Office of Naval Research, Dept. of the Navy, 500 N. Quincy St., Arlington, VA 22217	12. REPORT DATE: November 1984
	13. NUMBER OF PAGES
14. MONITORING AGENCY NAME & ADDRESS(if different from Controlling Office)	15. SECURITY CLASS. (of this report): Unclassified
	15a. DECLASSIFICATION DOWNGRADING SCHEDULE

16. DISTRIBUTION STATEMENT (of this Report)

Approved for public release; distribution unlimited

17. DISTRIBUTION STATEMENT (of the abstract entered in Block 20, if different from Report)

JAN 10 1985

D

A

18. SUPPLEMENTARY NOTES

19. KEY WORDS (Continue on reverse side if necessary and identify by block number)

20. ABSTRACT (Continue on reverse side if necessary and identify by block number)

A clean Fe(001) unreconstructed surface has been analyzed using low energy ion scattering with time of flight energy analysis. The intensity of scattered 9.5 KeV Ne^+ ions and neutrals was measured as a function of elevation and azimuth of the incoming beam while keeping a fixed scattering angle of 90^0. The observed intensity variations can be described by considering the shadowing and blocking of the second and third atomic layers. A simple Firsov potential was used to calculate the shadow cone dimensions. The good agreement between the observed and calculated variations in scattered

DD FORM 1 JAN 73 1473 EDITION OF 1 NOV 65 IS OBSOLETE
S/N 0102-014-6601

SECURITY CLASSIFICATION OF THIS PAGE (When Data Entered)

intensity demonstrates the utility of this relatively simple technique for preliminary analysis of surface structure.

Surface Science 141 (1984) 549–566
North-Holland, Amsterdam

SURFACE STRUCTURE ANALYSIS USING LOW ENERGY ION SCATTERING
I. Clean Fe(001)

L. MARCHUT, T.M. BUCK, G.H. WHEATLEY and C.J. McMAHON, Jr. *
AT&T Bell Laboratories, Murray Hill, New Jersey 07974, USA

Received 9 August 1983; accepted for publication 28 February 1984

A clean Fe (001) unreconstructed surface has been analyzed using Low Energy Ion Scattering with time of flight energy analysis. The intensity of scattered 9.5 KeV Ne^+ ions and neutrals was measured as a function of elevation and azimuth of the incoming beam while keeping a fixed scattering angle of 90°. The observed intensity variations can be described by considering the shadowing and blocking of the second and third atomic layers. A simple Firsov potential was used to calculate the shadow cone dimensions. The good agreement between the observed and calculated variations in scattered intensity demonstrates the utility of this relatively simple technique for preliminary analysis of surface structure.

1. Introduction

The Low Energy Ion Scattering (LEIS) technique utilizes a beam of mono-energetic ions as a probe of the surface and can be used for elemental identification, quantitative analysis and surface structure analysis. When a beam of accelerated ions strikes a crystal surface, many of the ions make elastic collisions with target atoms. The energy of an ion making such an elastic collision, here expressed as the ratio of final energy, E_1 to initial energy, E_0 can be derived using energy and momentum conservation laws as:

$$E_1/E_0 = \left[M_1^2/(M_1+M_2)^2\right]\left[\cos\theta_L + \left(M_2^2/M_1^2 - \sin^2\theta_L\right)^{1/2}\right]^2. \quad (1)$$

Here M_1 is the mass of incoming ion, M_2 the mass of the target atom and θ_L the laboratory scattering angle. By measuring the energy distribution of scattered particles the elements present in the region sampled by the ion beam can be determined in a straighforward manner. This is illustrated in fig. 1 which is a spectrum for 9.5 keV Ne^+ ions and neutrals scattered from a Fe surface containing segregated Sn. (The Fe–3.9at%Sn single crystal used for this study could be sputtered and annealed at 500–600 °C resulting in an ordered

* Department of Materials Science and Engineering, University of Pennsylvania, Philadelphia, Pennsylvania 19104, USA.

0039-6028/84/$03.00 © Elsevier Science Publishers B.V.
(North-Holland Physics Publishing Division)

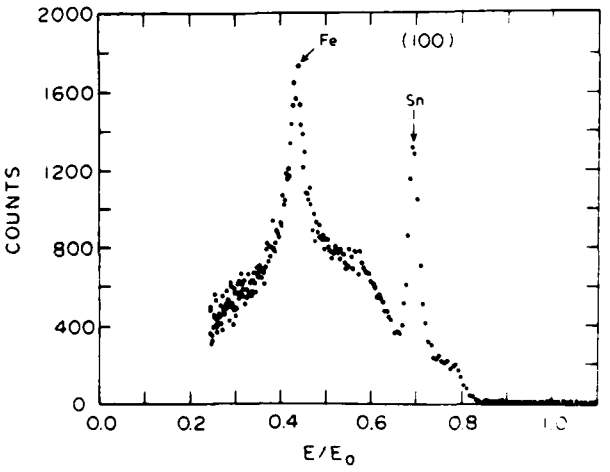

Fig. 1. Typical Time-of-Flight LEIS energy spectrum derived from TOF distribution 9.5 keV Ne^+ scattered from an Fe–Sn single crystal, (001) surface, with segregated Sn.

surface layer enriched in Sn, or sputtered and annealed at 400 °C to remove damage due to sputtering but allow no Sn segregation. The analysis performed on the surface enriched in Sn will be the subject of a future paper.) Peaks are seen at $E/E_0 = 0.43$ and 0.70 due to scattering through 90° from Fe and Sn. This energy spectrum was derived from a time-of-flight (TOF) spectrum which was calibrated with reference to 90° scattering of Ne^+ from Sn using a Tennelec TC850 time calibrator. The discrepancies in the observed peak positions and those calculated from eq. (1) probably arise from inelastic energy loss and systematic errors in the time calibration. Such discrepancies are unimportant to the analysis presented here. The background in this figure is from ions which scattered from more than one target atom before leaving the crystal.

The LEIS (TOF) technique used in this study allows detection of both ions and neutrals, avoiding complications due to neutralization effects [1,2] which must be considered if an electrostatic analyzer (ESA) is used. A weakness of the LEIS (ESA) technique is that many ion-target collisions will result in displacement and removal of surface atoms. The ion dose required by the LEIS (TOF) technique is 100–1000 times smaller than for the LEIS (ESA) method using noble gas ions for two reasons: (a) both scattered ions and neutrals are collected and (b) LEIS (TOF) is a multi channel technique collecting at all energies concurrently rather than sequentially as with an ESA. At low energies the scattering cross sections are relatively large, allowing more rapid data accumulation than is possible at high energies. In addition the large scattering

cross sections lead to strong attenuation of the incoming and outgoing particles so that analysis can be limited to the top atomic layer [3].

In this and many previous LEIS studies [4–11] information about the arrangement of adsorbed atoms on the surface has been obtained by taking advantage of the shadowing effect. This occurs because ions approaching a target atom are deflected away from it, with the ions approaching more closely being deflected the most. As a result the beam does not penetrate a region called the shadow cone behind each target atom as shown in fig. 2. By comparing changes in measured scattered intensity with the projections of shadow cones on different atoms, the arrangement of atoms on the surface can be deduced.

2. Experimental procedure

The LEIS measurements were performed in a system described previously [1,12–14], a diagram of which is shown in fig. 3. The cryo-pumped UHV chamber reached an ultimate pressure of about 2×10^{-10} Torr, with the pressure increasing to about 2×10^{-9} Torr due primarily to Ne during the ion scattering measurements. The chamber was equipped with a LEED–AES system and an ion gun (both from Physical Electronic Industries, Inc.), in addition to the ion-scattering facilities.

The sample was mounted on a (Varian) heater and sample temperature was measured using a chromel–alumel thermocouple spot-welded to a Ta clamp which held the sample onto the heater. The heater and sample were mounted on a manipulator that allowed three translational motions with a reproducibility of ± 1 mm and rotation about two axes accurate to $\pm 1°$.

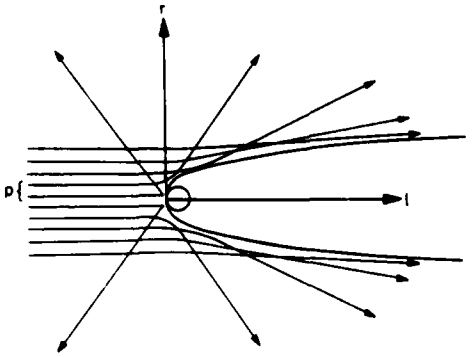

Fig. 2. Sketch showing the general relationship between the trajectory of scattered particles and impact parameter p, and the formation of a shadow cone.

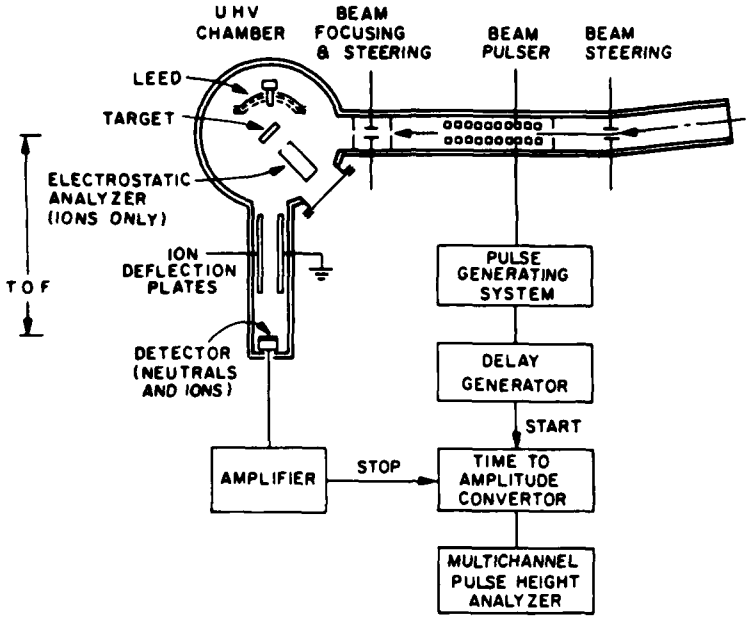

Fig. 3. Diagram of the system used for LEIS measurements.

The ion scattering was performed using a pulsed 9.5 keV beam of Ne^+ ions. Scattered particles, both ions and neutrals, were collected by a Johnston Multiplier ~ 1.0 m from the sample and oriented at a scattering angle θ of 90°. Time-of-flight energy analysis of scattered particles was used to that both ions and neutrals were collected, avoiding complications due to neutralization effects mentioned earlier. The time resolution of the system was about 60 ns. For 9.5 keV Ne^+ scattering from Fe at 4.47 keV and 4.5 μs time of flight this corresponds to an energy resolution of 0.3 keV or $\Delta E/E \sim 0.026$.

The sample studied was from an Fe–1.65at%Sn alloy which had been directionally solidified, resulting in large collumnar grains which were homogenized at 950°C for 75 h *. A single crystal with a (001) surface was spark-cut from the ingot. An optically flat surface was prepared by mechanical polishing using alumina powders, followed by Syton (TM) polishing (0.01 μm alumina suspended in NaOH) and etching with dilute nitric and glacial acetic acid leaving a damage free surface.

The crystal surface was cleaned further inside the vacuum chamber by argon

* Alloy prepared through the courtesy of Dr. C.L. Briant of the General Electric Research and Development Center Schenectady.

ion sputtering (0.5 kV, 10 μA) with the sample at 400 °C, followed by a 30 min anneal at 400 °C to eliminate damage due to sputtering. AES analysis of the sample at this point revealed the presence of some C and N which apparently had segregated to the surface during the 400 °C anneal and could not be completely removed by successive sputtering and annealing. The LEED pattern observed was essentially p(1 × 1) with faint split 1/2, 1/2 spots, probably due to C and N on the surface. A small amount of Sn also observed in both AES and LEIS spectra after the treatment described above. The Sn concentration was estimated to be 3.9 at%, representing only a slight enrichment of the surface.

3. Results and discussion

After cleaning of the sample, LEIS spectra were recorded for different orientations of the beam relative to the sample. The coordinates used to describe the beam orientation are shown in fig. 4. The elevation angle of the beam relative to the sample surface is designated ψ, with $\psi = 90$ normal to the surface. The azimuthal angle, ϕ, is the angle of rotation about the surface normal, with $\phi = 0$ being parallel to a (110) plane. For clarity, when the beam is aligned parallel to a low index plane of the crystal, the indices of this plane will be used to define the azimuth.

If relative intensities were compared using peak heights without background subtraction, the change in background due to multiple scattering (which is large for some orientations) would give spurious results. In addition the peak height may not accurately represent single scattering from deeper layers which primarily broadens the peak. To avoid these problems, relative intensities were compared using integrated peaks after subtracting the multiple scattering

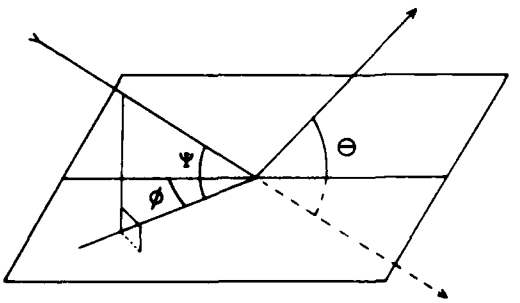

Fig. 4. Coordinates used to describe scattering of an ion by a surface atom. ψ is the elevation of the incoming beam above the plane of the surface, ϕ is azimuthal angle or angle of rotation about the surface normal with respect to some reference plane and θ is the scattering angle.

background. The area integrated was that within the single scattering peaks, with the subtracted background being the average of the number of counts at the two limits of integration, multiplied by the width of the peak. The single scattering peaks shown in fig. 1 (which represents a (110), 35° beam orientation) have clear limits; the transition between the peak and background is sharp and a small change in the limits of integration would not effect the sum appreciably. However, for some beam orientations this was found not to be true. Fig. 5 shows a spectrum from clean Fe with the beam at (210), 45° (azimuth parallel to (210) planes, elevation 45°). The multiple scattering yield is very large, and the limits of the single scattering peak are not obvious. The limits of integration for peaks such as this have been chosen to be reasonably close to those used for the sharp single scattering peaks, but it is obvious that this integration will have some inherent error. The broad shoulders on the low and high energy sides of the Fe single scattering peak in figs. 1 and 5 are probably due to multiple scattering sequences involving several atomic layers which neutralize the ions quite completely so that such structure does not show up very strongly in ESA spectra. Identification of such sequences has been made by computer simulation for another system, $Cu_3Au(100)$ [15,16].

A correction must be made to the integrated intensities measured at different elevations. The spot size of the beam on the sample depends on the elevation angle; the intensities were multiplied by $\sin(\psi)$ to correct for this.

Sequences of spectra were recorded at ~4° intervals of rotation of the

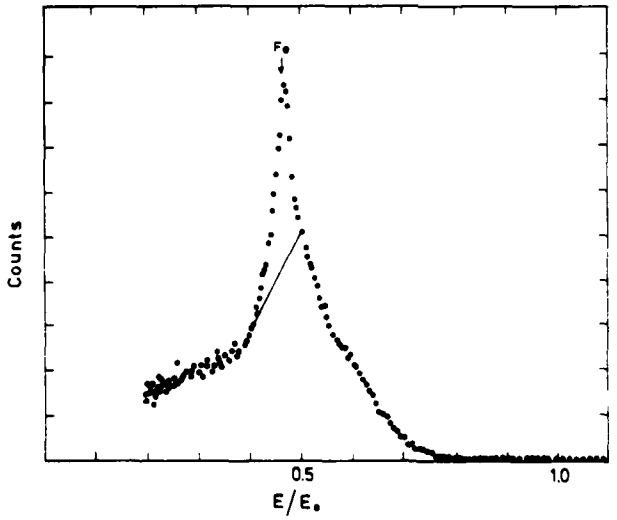

Fig. 5. LEIS spectrum from the clean surface with the beam oriented parallel to (210) planes. $\psi = 45°$.

crystal about its normal at fixed elevation angles, or at 2.5–5° steps of elevation with fixed azimuthal angles. The data from the azimuthal and tilt scans have been combined in plots of scattered intensity versus ψ and ϕ, which will be called intensity plots (e.g. fig. 6).

Ideally, these data would be plotted as contour maps with contours of different scattered intensity shown, but measurements were not made at enough orientations to do this accurately. The intensity plots show the sum of each single scattering peak multiplied by $\sin(\psi)$ and rounded off to the nearest thousand counts. This averages out fluctuations due to experimental error and allows the matching up of intentities where the scans intersect. Thus the intensity plots show only the larger intensity variations and not the finer details of the same order of magnitude as the experimental error.

The intensity distributions were plotted for ψ from 0° to 90° and from $\phi = 0°$ (a (110) azimuth) to $\phi = 45°$ (a (100) azimuth). The limits reflect both

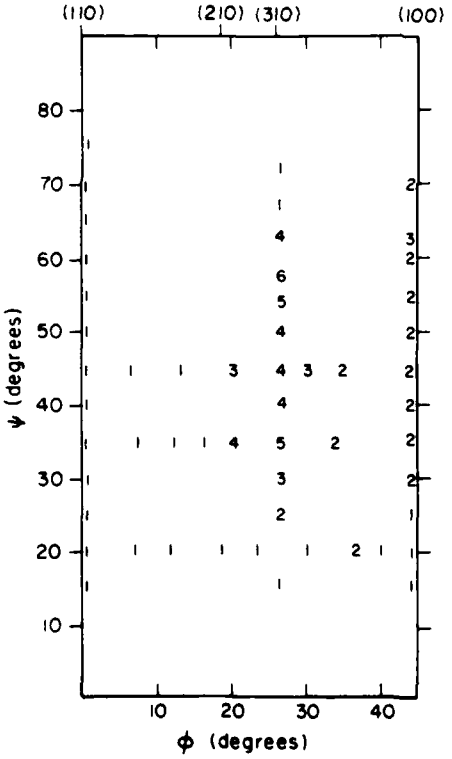

Fig. 6. Intensity map showing the relative intensities (counts/1000) of the Fe single scattering peaks as a function of ψ and ϕ from the clean Fe surface.

the possible range of ψ for 90° scattering and the range of ϕ necessary to represent the bcc (001) surface. The intensity plot for the clean Fe surface is shown in fig. 6 and comprises data from azimuthal scans at $\psi = 20°$, 35° and 45° and from tilt scans along (110), (310) and (100) planes. The lowest intensities (~ 1000 counts) are seen near the (110) azimuth where only the first layer is visible to the beam. Apparently, single scattering from the second layer does not occur at any elevation along this azimuth. This is in agreement with the shadow cone analysis to be discussed below. The single scattering intensities are roughly twice as large near the (100) azimuth, showing little change with elevation. The highest intensities are seen near the (310) azimuth at elevations between 35 and 60 degrees.

This intensity plot will be discussed in the following section where the changes in scattered intensity are compared with changes in the number of atoms visible to the beam as predicted by a shadow cone analysis.

4. Shadow cone analysis

As mentioned previously, when a beam of ions is incident on an atom, there will be a region beyond the atom into which the ions cannot penetrate. The formation of this region can be understood with the help of fig. 2. A target atom is shown, and trajectories of scattered ions are shown schematically. The scattering angle and energy loss of an ion due to a scattering event can be expressed in terms of an impact parameter, p, which is the distance of closest approach the ion and target atom would have if no scattering occurred. The ions with small impact parameters are scattered through large angles while ions with large impact parameters are deflected only slightly. The net result is that the ions do not penetrate a region beyond the target atom. If the scattering angle is known as a function of impact parameter, the dimensions of this region, called the shadow cone, can be calculated.

The shadow cone dimensions used here have been calculated in the manner of Martynenko [17,18] who applied a shadow cone analysis to single crystal sputtering. The calculations are fairly simple for the interaction potential used, which is of the form $V(x) = A/x^2$, where A includes the part of the screening function which is independent of x. If the potential is used, and it is further assumed that near the edge of the shadow cone the ions are scattered through small angles since the ions and target atom do not approach closely, the scattering angle, θ, and impact parameter, p, are related by a simple analytical expression. Using this relation, Martynenko derived the following formula for the radius, r, of the shadow cone at a distance, l, beyond the target atom.

$$r = 2.2\left(lA/(\mu + 1)E_0\right)^{1/3}. \tag{2}$$

Here μ is the ratio of the mass of the incident ion to that of the target atom.

The potential used by Martynenko is the approximation to the Thomas–Fermi potential by Firsov [19]. Firsov showed that in the energy range 1–50 keV the following screened coulomb potential is within 10% of the Thomas–Fermi potential:

$$U(r) = \frac{Z_1 Z_2 e^2}{x}\left(\frac{0.45}{x} R_s\right), \tag{3}$$

where Z_1 and Z_2 are the atomic numbers of the ion and target atoms and e is the the electronic charge. The bracketed term is Firsov's screening function, with R_s being the screening radius:

$$R_s = (9\pi^2/128)^{1/3}\, a_0 (Z_1^{1/2} + Z_2^{1/2})^{-2/3}, \tag{4}$$

where a_0 is the Bohr radius $\hbar^2/me^2$.

The Firsov potential was used to calculate the shadow cone dimensions in this study, with one minor correction. It has been shown [11] that, if the above screening radius is multiplied by 0.8 and used in the Molière approximation to the Thomas–Fermi potential, the ratio of single to double scattering for computer simulation of 2.5 keV Ne^+ scattering from Au and Ni is in good agreement with experimental results. This same correction has been applied to the Frisov potential used in this study, so the potential constant A is given by:

$$A = 2.44 Z_1 Z_2 / (Z_1^{1/2} + Z_2^{1/2})^{2/3}\ \text{eV Å}^2, \tag{5}$$

Fig. 7 shows shadow cones calculated for 9.5 keV Ne^+ on Fe projected on an Fe lattice. The second layer atoms in this figure are inside the shadow cones of

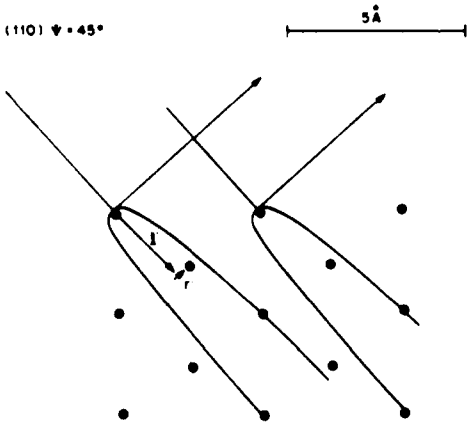

Fig. 7. Shadow cones calculated for 9.5 keV Ne^+ scattering from Fe projected onto an Fe(110) plane for $\psi = 45°$ showing the shadowing of the second layer by the first.

first layer atoms and therefore should not contribute to the scattered intensity.

Using the shadow cone dimensions given by eq. (2), the ranges of ϕ and ψ for which any atom in the crystal will shadow another can be calculated. This was done in the following manner. A pair of atoms was chosen and the coordinates of one with respect to the other were calculated from the lattice parameter. The shadow cone was projected on these atoms with the shadowing atom at the apex and its central axis parallel to the incoming beam direction. A plane perpendicular to the beam direction which contained the shadowed atom was also considered. The distance l' from the shadowing atom to this plane (see fig. 7) and distance r' in this plane from the shadowed atom to the central axis of the shadow cone were then calculated. The distance r' was then compared with $r(l')$ calculated using eq. (2) to see if the atom is inside the shadow cone. For each pair of atoms chosen the limits of ψ corresponding to the atom's being at the edges of the shadow cone were determined within $\pm 1°$ using an iterative search technique. This was done at $5°$ increments of ϕ from $\phi = 0$ to $\phi = 45°$, so that the shadowing and blocking limits for ϕ rotations were also determined. These limits were then plotted on a ϕ–ψ plot, so that minima in the scattered intensity (e.g. fig. 6) could be compared with beam orientations for which deeper layers are shadowed.

This solution gives results slightly different from those of Bronckers and De Wit [8], who plotted the shadowing limits as circles of radius $\Omega = (180/2\pi)\tan^{-1}(r'/l')$ with r' and l' determined for the two atoms aligned along the central axis of the shadow cone. Bronckers and De Wit ignore the variation of l' when the shadowed atom is not on the central axis of the shadow cone; this is a good approximation if $l \gg r$ or if the radius of the shadow cone is not a strong function of l.

If the crystal is oriented so that the second layer is exposed to the beam, it is still possible that the second layer atoms will not contribute to the scattered intensity. Ions scattered by second layer atoms can be deflected or blocked by atoms in the first layer on the way out, so that they do not reach the analyzer. An analysis of blocking cones has been done for experiments in which the incident ion beam was kept at a fixed elevation and variations in intensity were monitored by moving the detector independently [20,21]. As shown in fig. 8, the ion beam reaches an atom in the second (or deeper) layer and scatters from it over a range of angles, θ_1. This atom can be considered to be a point source of ions of various energies $E(\theta_1)$ given by eq. (1) with $\theta_L = \theta_1$. As the ions pass the blocking atom they will scatter from it at different angles, θ_2, which will depend on $E(\theta_1)$ and their impact parameters with this atom which are also a function of θ_1. As in the case of shadowing, an ion will scatter through large angles if it approaches the blocking atom at small impact parameters and small angles for large impact parameters. The edges of the blocking cone correspond to scattering conditions for which

$$d(\theta_1 + \theta_2)/d\theta_1 = 0,$$

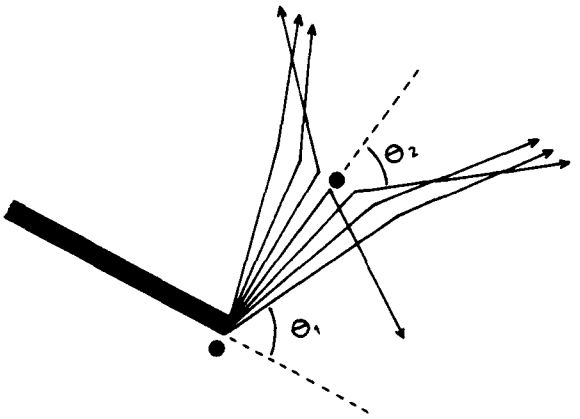

Fig. 8. The trajectories of ions scattered from an atom, showing blocking by a second atom.

where

$\theta_2 = f(\theta_1)$.

If the Firsov potential described previously is used, the angular half width of the blocking cone, δ is given by:

$$\delta = 2.2\left[A/E(\theta_1)d^2\right]^{1/3}, \tag{6}$$

where d is the distance between the two atoms along the central axis of the blocking cone. A simplification is possible for the experiments reported here, since the total scattering angle is held constant at $\theta = 90°$. Hence that $E(\theta_1)$ is given by the solution to eq. (1) for this scattering angle:

$$E_1/E_0 = (M_2 - M_1)/(M_2 + M_1). \tag{7}$$

For each pair of atoms chosen, the distance, d, from the blocked atom to the blocking atom was calculated and used in eq. (6) to calculate δ, the half width of the blocking cone. The region for which blocking occurs was plotted directly on the ϕ–ψ diagram as a cirle of radius δ.

5. Analysis of scattering from the clean Fe surface

The applicability of the shadow cone analysis is demonstrated here by using it to determine the beam orientations for which atoms in the second and third layers of the clean (001) Fe surface are not shadowed or blocked. These orientations can then be compared with the beam orientations that have high measured scattered intensity in the map for clean Fe.

For an unreconstructed Fe surface, all atoms in the second layer are equivalent so that shadowing and blocking of only one second layer atom need to considered. The regions of ϕ–ψ space for which this atom is shadowed by any of five nearby first layer atoms have been calculated, along with regions for which five equivalent atoms block the outgoing ions. The atoms chosen are indicated in fig. 9, which shows the top two crystal layers as seen from above. The beam is assumed to be incident so that the atoms labeled 1S...5S will shadow the atom marked 0, and the atoms labeled 1B...5B will block ions scattered from this atom.

The coordinate system (ϕ–ψ) used for these calculations is the same as the one used experimentally, and the range of ϕ shown in fig. 9 is the same as that used for the intensity plots. Because of the symmetry of unreconstructed Fe

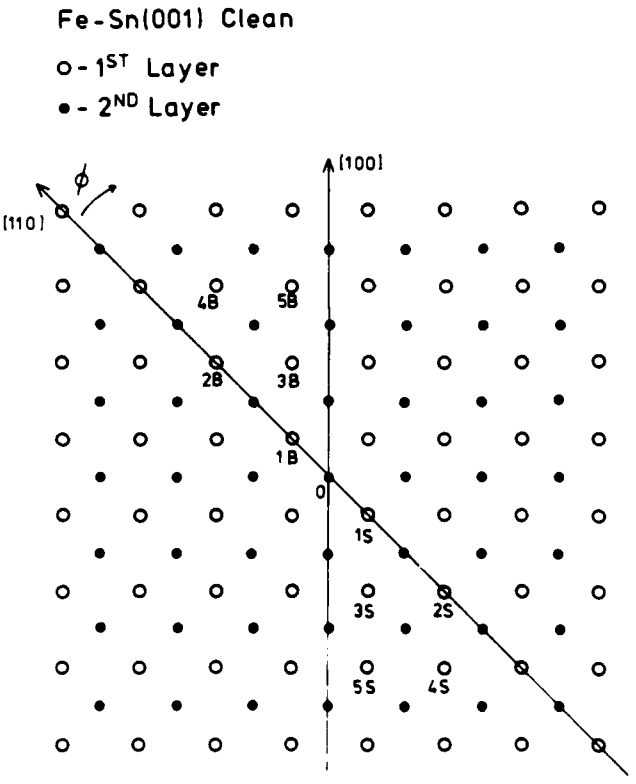

Fig. 9. Top view of the Fe (001) surface showing first and second layer atoms as light and dark circles. Atoms whose shadowing or blocking of the second layer atom marked 0 have been considered are labeled.

(001) surface, this range of ϕ (45°, from a (110) azimuth to a (100) azimuth) is sufficient to describe all possible ϕ. Within the range of ϕ considered, first layer atoms other than those labeled, and some second layer atoms, will shadow and block the second layer atom being considered, but only at ψ less than 15° or greater than 75°. These were chosen as limits of ψ for which shadowing and blocking cones needed to be calculated, since no data were collected outside this region.

On a ϕ–ψ plot the shadowing limits for each first layer atom are distorted circles, while the blocking limits are circles. For simplicity the shadowing and blocking limits in regions where these circles overlap were not included. The limits of these combined shadowing and blocking cones are plotted in fig. 10. The hatched region corresponds to ϕ and ψ for which the second layer of the crystal is shadowed or blocked by the first. For comparison the experimental

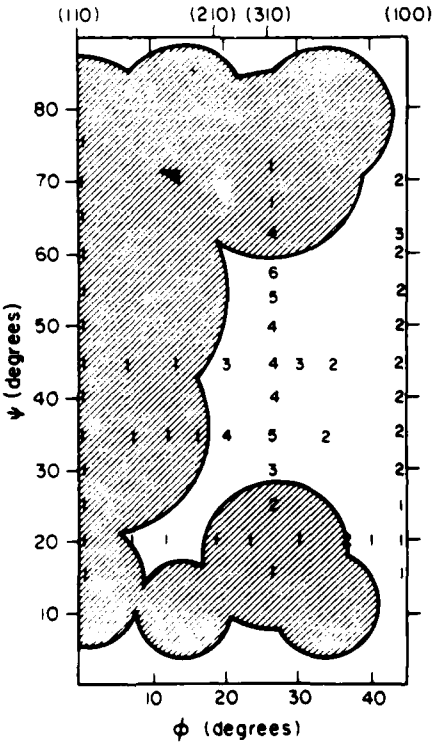

Fig. 10. Plot of shadowing and blocking limits in ϕ and ψ for first layer Fe atoms on the 2nd layer. Regions where the second layer is hidden are shown hatched. For comparison an intensity map (in counts/1000) for Ne^+ scattering from clean Fe is also shown.

clean Fe intensity plot is also shown on this figure. The lowest scattered intensities are observed in regions where the second layer is not visible, according to the calculation. It should be emphasized that single scattering only has been considered here. Multiple scattering may occur within the shaded regions, but the multiple scattering background has been subtracted as described earlier.

An effect not satisfactorily explained by shadowing and blocking of the second layer is the large increase in scattered intensity from clean Fe near the (310) azimuth for $35 < \psi < 62.5$. This might be explainable in part as a focussing effect, but the greatest focussing would be expected near the edges of the shadow cones and it is not expected to persist far beyond this. Thus, focussing would not explain the increased intensity seen near $\psi = 45°$, $\phi = 27°$ in fig. 10. A similar analysis has therefore been done to see if the third layer is

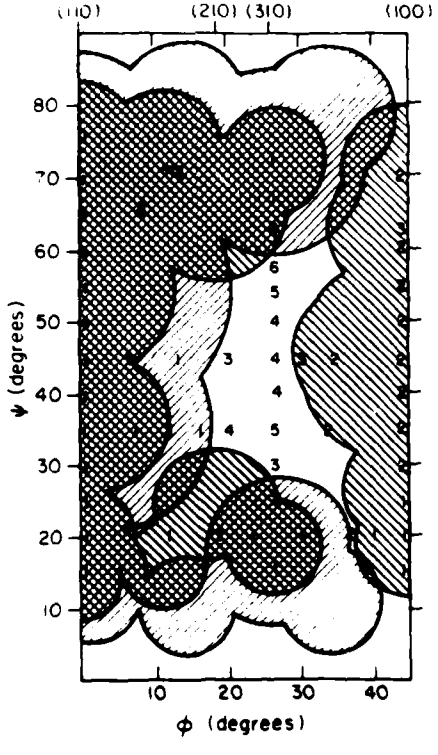

Fig. 11. Plot of regions where third layer atoms are hidden by first layer atoms (\\\\) and second layer atoms (////) as a function of ϕ and ψ. For comparison an intensity map for Ne^+ scattering from clean Fe is also shown.

visible to the beam at any of the beam orientations studied. As with the second layer analysis, only one third layer atoms need be considered, but shadowing and blocking of this atom by both first and second layer atoms must be included. The regions in which second layer atoms shadow and block the third layer atom are identical to those for which first layer atoms shadow and block the second layer, as shown in fig. 10. Regions in which a third layer atom is shadowed and blocked by first layer atoms were calculated in a manner similar to that described above. These regions are shown hatched with lines of positive slope (\\\\) in fig. 11. Also shown are the shadowing and blocking regions due to atoms in the second layer, hatched with lines of negative slope (////). As noted previously, these regions are the same as the shadowing and blocking limits for first-layer atoms on a second-layer atom. In fig. 11 areas hatched with positive slope correspond to regions where only the first layer is visible; areas hatched only with negative slope correspond to regions where both the first and second layers are visible, and for areas with no hatching the first, second, and third layers should be visible.

An intensity map for Ne^+ scattering from the clean Fe surface is also plotted in fig. 11. The regions of highest scattered intensity (> 4000 counts) correspond reasonably well to unhatched areas in this figure where atoms in the first, second, and third layers should be visible. The regions of lowest intensity ($\leqslant$ 1000 counts) coincide with regions for which only the top layer is visible (hatching with positive slope).

The most notable disagreement is near the (310) azimuth ($\phi = 27°$) for $\psi = 25°$ and $\psi = 62.5°$. A better fit to the data would be observed if the interatomic potential were modified to give slightly smaller shadow cones. Another possibility is that the potential is correct but the outermost atomic planes are displaced inwards so that the third layer is exposed to the beam over a larger angular range. It is also possible that some multiple scattering sequence contributes to the peak at $E_1/E_0 \approx 0.47$, an effect not considered in this single scattering analysis. Computer simulation of the particle trajectories will be needed to clarify this matter.

Estimates of the limits of error which could be introduced by the neglect of certain other effects in this analysis are illustrated in fig. 12 which shows a shadow cone calculated for 9.465 keV Ne^+ scattered from Fe from two atoms spaced as in an Fe(110) plane. Firsov estimated that his potential was within $\pm 10\%$ of the Molière approximation to the Thomas–Fermi potential which is generally accepted for low energies. The thickness of the line drawn to represent the shadow cone reflects this uncertainty. This error is fairly small, since $r(l)$ varies as $A^{1/3}$.

Another error in the shadow cone analysis arises in that the shadowed atom in fig. 12 is assumed to become visible when it reaches the edge of the shadow cone. Actually, since the collected ions scatter through 90° from the target atom, they have approached it at a small impact parameter. This means that

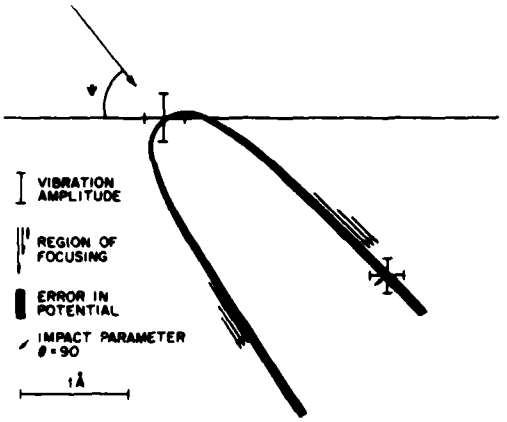

Fig. 12. Shadow cone calculated for 9.5 keV Ne^+ scattering from Fe showing the magnitude of various sources of error in this analysis. The error in the potential refers to the discrepancy between the dimensions calculated using the Firsov and Molière-Thomas-Fermi potentials.

the ions will scatter from this atom when it is still inside the shadow cone by the present definition. Calculations by Chen [22] indicate that the impact parameter for 90° scattering of 9.5 keV Ne^+ on Fe is about 0.1 Å. This distance is shown as an arrow at the shadowed atom in fig. 12, and the result is that the shadow cone calculated is 2° or 3° too large.

There will be some uncertainty about the positions of both the shadowing and shadowed atom due to vibrations. The error bars in fig. 12 indicate expected rms vibration amplitudes of the atoms. These were taken from calculations of Gupta and Hemkar [23] which were based on the variation of the Debye-Waller factor with temperature [24], and theoretical predictions of Dobrzynski and Masri [25] from the elastic constants of Fe. The effect of vibrations will be to superimpose a Gaussian distribution on the step function that might otherwise to be expected to describe the change in intensity near the edge of a shadow cone.

Another change in scattered intensity near the edge of the shadow cone will be enhancement of the intensity just outside the shadow cone due to focussing. This occurs as many incoming ions are deflected through small angles away from the shadowed region and into the nearby region just outside the shadow cone, so that an atom in this region receives a higher than average flux. The expected width of the region of enhanced intensity is indicated by the arrows just outside the shadow cone in fig. 12 and is taken from De Wit and Bronckers [7], who calculated the distribution of 5 keV Ne^+ ions scattered by a Cu atom using an A/r^2 potential similar to the one used here.

This analysis of the clean Fe(001) surface demonstrates that LEIS can be

used for layer by layer chemical analysis of unreconstructed surfaces since sample orientations at which different layers are exposed to the ion beam can easily be predicted. The focussing factors for each individual layer should be determined if possible when performing such an analysis. A similar analysis [26] has been done for an ordered Cu_3Au (001) surface and good agreement between measured and predicted intensity variations with sample orientation were also observed. Another possible application of the shadow cone analysis is to test various models of reconstructed surfaces.

Acknowledgements

This research was done while one of the authors (L. Marchut) was a graduate student at the University of Pennsylvania and was supported as a Resident Visitor at Bell Laboratories. The research at the University of Pennsylvania was supported by the office of Naval Research under Grant No. N-0014-79-CO991. The authors would also like to thank Doyle Temple of Southern University for help with data collection.

References

[1] T.M. Buck, G.H. Wheatley, G.L. Miller, D.A.H. Robinson and Y.S. Chen, Nucl. Instr. Methods 149 (1978) 591.
[2] S.B. Luitjens, A.J. Algra, E.P. Th. M. Suurmeijer and A.L. Boers, Appl. Phys. 21 (1980) 205.
[3] T.M. Buck, G.H. Wheatley and L.K. Verheij, Surface Sci. 90 (1979) 635.
[4] W. Heiland and E. Taglauer, J. Vacuum Sci. Technol. 9 (1972) 620.
[5] W. Heiland, F. Iberl, E. Taglauer and D. Menzel, Surface Sci. 53 (1975) 383.
[6] H.H. Brongersma and J.B. Theeten, Surface Sci. 54 (1976) 519.
[7] A.G.J. de Wit, R.P.N. Bronckers and J.M. Fluit, Surface Sci. 82 (1979) 177.
[8] R.P.N. Bronckers and A.G.J. de Wit, Surface Sci. 104 (1981) 384.
[9] R.P.N. Bronckers and A.G.J. de Wit, Surface Sci. 112 (1981) 111.
[10] R.P.N. Bronckers and A.G.J. de Wit, Surface Sci. 112 (1981) 133.
[11] T.M. Buck, I. Stensgaard G.H. Wheatley and L. Marchut, Nucl. Instr. Methods 170 (1980) 519.
[12] T.M. Buck, Y-S Chen, G.H. Wheatley and W.F. Van der Weg, Surface Sci. 47 (1975) 244.
[13] G.H. Wheatley and C.W. Caldwell, Rev. Sci Instr. 44 (1973) 744.
[14] Y.S. Chen, G.L. Miller, D.A.H. Robinson, G.H. Wheatley and T.M. Buck, Surface Sci. 62 (1977) 133.
[15] D.P. Jackson, T.M. Buck and G.H. Wheatley, Nucl. Instr. Methods B2 (1984) 440.
[16] T.M. Buck, G.H. Wheatley and D.P. Jackson, Nucl. Instr. Methods, to be published.
[17] Yu. V. Martynenko, Soviet Phys.-Solid State 6 (1965) 1581.
[18] Yu. V. Martynenko, Soviet Phys.-Solid State 6 (1965) 2827.
[19] O.B. Firsov, Soviet Phys.-JETP 34 (1958) 308.
[20] E.S. Mashkova and V.A. Molchanov, Radiation Effects 25 (1975) 33.
[21] W.C. Turkenburg, W. Soska, F.W. Saris, H.H. Kersten and B.G. Colenbrander, Nucl. Instr. Methods 132 (1976) 587.

[22] The computer program for scattering cross-sections was written by Y.S. Chen of Bell Telephone Laboratories and was based on an analysis of M.T. Robinson and I.M. Torrens, Phys. Rev. B9 (1974) 5008.
[23] O.P. Gupta and M.P. Hemkar, Z. Naturforsch. 32a (1977) 1495.
[24] P. Debrunner and R.J. Morrison Rev. Mod. Phys. 36 (1964) 463.
[25] L. Dobrynski and P. Masri, J. Phys. Chem. Solids 3 (1972) 1603.
[26] T.M. Buck, G.H. Wheatley and L. Marchut, Phys. Rev. Letters 51 (1983) 43.

END

FILMED

2-85

DTIC